
# Au-Pd Barcode Nanowires with Tailored Lattice Parameters and Segment Lengths for Catalytic Applications

ACS APPLIED NANO MATERIALS

Open Access



www.acsanm.org

Article

# Au–Pd Barcode Nanowires with Tailored Lattice Parameters and Segment Lengths for Catalytic Applications

Giuseppe Abbondanza,* Andrea Grespi, Alfred Larsson, Crispin Hetherington, Matthew Snelgrove, Francesco Carlá, Nikolay Vinogradov, Roberto Felici, and Edvin Lundgren

Cite This: *ACS Appl. Nano Mater.* 2024, 7, 3861–3872

Read Online

ACCESS | Metrics & More | Article Recommendations | Supporting Information

**ABSTRACT:** In this study, we present a systematic investigation of the controlled fabrication of Au–Pd barcode nanowires within nanoporous anodic aluminum oxide (NP-AAO) templates. By using a combination of *in situ* X-ray diffraction (XRD), focused ion beam scanning electron microscopy (FIB-SEM), and transmission electron microscopy (TEM), we elucidate the influence of template preparation methods on the resulting nanowire properties. The template treatment, involving either pore widening or barrier layer thinning, significantly impacts nanowire growth. Through the analysis of the XRD data, we observe sequential deposition of Au and Pd segments with lattice parameter variations and strain effects. Particularly, the lattice parameters of Au and Pd segments display intricate temporal dependencies, influenced by interfacial effects and strain caused by growth under confinement. FIB-SEM imaging reveals uniform and reproducible nanowire lengths in the template treated with pore widening. Furthermore, TEM analysis confirms the presence of distinct Au and Pd segments, while scanning TEM–energy-dispersive X-ray spectroscopy revealed minor evidence of interdiffusion between the first and the second electrodeposited segments. Our findings emphasize the potential of the electrodeposition process within nanoporous templates for producing barcode nanowires with precise segmental properties. The combination of *in situ* XRD and electron microscopy offers valuable insights into the growth dynamics and structural characteristics of the fabricated Au–Pd barcode nanowires. This controlled fabrication strategy opens doors to tailoring nanowire properties for diverse applications, particularly in catalysis.

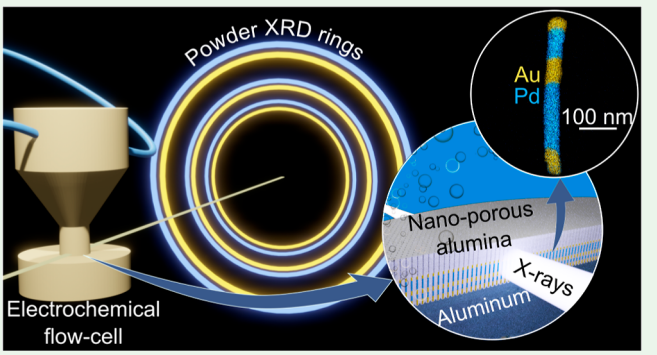


**KEYWORDS:** *gold, palladium, nanomaterials, multisegmented, barcode, synchrotron, X-ray diffraction, electrodeposition*



## INTRODUCTION

Nanostructures incorporating multimetallic components have been a subject of considerable interest due to their unique properties and outstanding performance arising from the synergistic interaction between the metal components.[1−5] The prominent examples of such nanostructures based on two or more metals could include nanoalloys,[6,7] heterostructures, such as core–shell nanoparticles,[8,9] barcode nanorods, and nanowires.[10−13]

Among the many synthetic routes to fabricate "barcode" nanowires (often referred to as multisegmented or segmental nanowires), we find the seeded growth[3,14] and the hard template method.[10] In seeded growth, achieving a specific morphology and structure depends on various factors like growth kinetics, thermodynamics, capping agents, lattice mismatch, and seed structure.[15−18]

While seeded growth has a high yield, in some cases, it requires capping agents, necessitating a decapping stage.[19] Moreover, nanostructures are restricted to three segments like M-Au-M (M being Pd or Ag).[14,17,20] To overcome these limitations, the hard template method can be used.[21] Electrodeposition of metals in hard templates such as nanoporous anodic aluminum oxide (NP-AAO) allows fabrication of ordered arrays of nanostructures without surfactants or capping agents.[22,23] Although the yield is lower compared to seeded growth, there is no need for a decapping stage, and the number of segments is limited only by the template thickness. The nanowire aspect ratio and morphology depend on the pore radius, height, and template preparation method. Prior investigations of Au–Fe barcode nanowires have shown that adjusting the electrodeposition duration for each metal component can effectively control the lengths of the segments.[24] While Au–Fe or CoPtP nanowires find significant applications

Received: November 16, 2023
Revised: January 22, 2024
Accepted: January 24, 2024
Published: February 9, 2024

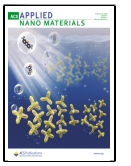

in magnetic storage media due to their high magnetic coercivity,[25] Au−Pd nanostructures are particularly well-known for their synergical importance in catalysis and electrocatalysis.[26,27]

Previous research indicates that nanostructures confined within NP-AAO experience lattice compression in the radial direction and elongation along the direction of growth. The amount of strain depends on the size of the template pore with smaller pores resulting in stronger stress. This effect could be put in a basis of engineering the nanomaterials with controllable strain characteristics.[28−30] The concept of artificially controlling strain is appealing, especially in catalysis, as it allows tuning the electronic structure and the chemisorption strength between late transition metals (such as Au and Pd) and adsorbates.[31−35]

While Au−Pd bimetallic nanostructures are promising catalysts,[36−40] there has been a lack of methods to monitor the segment lengths and the lattice parameters of Au−Pd nanocatalysts, while they are being fabricated. This important evaluation has often relied on *ex situ* measurements.[14,17,20,36−40] This study used NP-AAO templates for controlled Au−Pd barcode nanowire fabrication through alternating Au and Pd electrodepositions, as illustrated schematically in Figure 1.

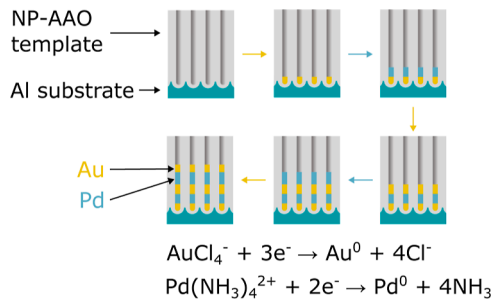


**Figure 1.** Illustration of the electrodeposition steps and reactions involved in the presented fabrication of barcoded Au−Pd nanowires.

Employing *in situ* X-ray diffraction (XRD), we observed two fcc phases corresponding to Au and Pd and lattice parameter variations due to confinement effects. The detection of the information encoded in the nanosegments is a prime challenge in this field, which has been addressed by multiple techniques such as X-ray fluorescence, square-wave voltammetry,[41] and photoluminescence.[42] In this work, we demonstrate that subtracting XRD patterns from consecutive segments provides structural insights into segments of the same type and their respective lengths.

For our electrochemical synthesis, two template treatments were employed: pore widening (PW) and barrier layer thinning (BLT). Both methods aim to reduce the insulating barrier layer at the pore bottom, enhancing the substrate conductivity for electrodeposition.[43] The preceding studies on Au and Pd electrodeposition demonstrated that these methods result in varied pore diameters and deposit morphologies.[22,23] We examine how template differences influence segment lengths and lattice parameters, showcasing more uniform and reproducible segment lengths in the pore-widened sample.

Some methods of templated multilayered nanowire fabrication[44] involve the detachment and the handling of the brittle and thin (e.g, 10−50 $\mu$m) NP-AAO from its aluminum matrix, the chemical removal of the barrier layer to achieve an open-pore structure, and the sputtering or evaporation of a noble metal (e.g., Au) to enable the electrochemical contact of the template with the solution. On the other hand, these steps are not necessary when utilizing PW and BLT.

Using focused-ion beam scanning electron microscopy (FIB-SEM), we determined the morphology of the nanomaterials and evaluated the segment lengths of the created Au−Pd nanowires. By selectively dissolving the NP-AAO, we could investigate the nanowires using transmission electron microscopy (TEM), scanning TEM−energy-dispersive X-ray spectroscopy (STEM-EDS), and selected area electron diffraction (SAED). This approach provided valuable insights into the local chemical composition and structure of the electrodeposited metal. By dissolving the NP-AAO template, the nanomaterials expose their surface to the surrounding environment, enabling their applications as catalysts.

## EXPERIMENTAL SECTION

**Template Preparation.** Two top-hat-shaped polycrystalline Al substrates with 6 mm diameter, purity 5N, and polished to an average roughness smaller than 0.03 $\mu$m (Surface Preparation Laboratory, The Netherlands) were cleaned by sonication consecutively in acetone, ethanol, and ultrapure $H_2O$. In this study, all electrolyte solutions were prepared using reagent-grade chemicals (Sigma-Aldrich) and ultrapure water (resistivity = 18.2 MΩ cm). The aluminum top-hats served as substrates for the NP-AAO template growth in a two-step anodization procedure.[45−47] First, these underwent anodization in 0.3 M $H_2SO_4$ at 25 V for 10 h while stirring, and the temperature was maintained at 0 °C through a jacketed electrochemical cell equipped with a refrigerated oil bath circulation. The anodization process was carried out using a programmable bipolar power supply (Kikusui PBZ-20-20). Then, the resulting NP-AAO was removed from the aluminum matrix by dissolving it via immersion in a water solution of 0.185 M $H_2CrO_4$ and 0.5 M $H_3PO_4$ for 14 h at room temperature. This step led to an aluminum substrate patterned with nanoconcaves.

The second anodization was conducted under identical conditions of electrolyte composition, applied potential, and temperature as the first anodization, although for different durations of either 30 or 20 min. For the samples subjected to a 20 min anodization, a technique known as BLT was applied as a treatment, which consisted of the decrease of the anodization potential from 25 to 1 V over 30 min. A PW step was performed on the samples anodized for 30 min by immersing them in a solution containing 0.5 M $H_3PO_4$ at a temperature of 30 °C. This immersion lasted for 6 min, with continuous stirring of the solution to mitigate convection effects. Immediately after all the anodization stages and after the PW, the samples were rinsed thoroughly in ultrapure $H_2O$ to avoid corrosive damage of the template. NP-AAO templates that underwent a BLT or PW treatment are referred to hereafter as BLT templates and PW templates, respectively. The same BLT and PW procedures described here have been used in previous research for the electrodeposition of Au and lead to pore diameters, hence nanowire diameters, of 25 and 46 nm, respectively.[22]

**Electrodeposition of Au−Pd Nanowires.** The templates were introduced in the PEEK electrochemical flow-cell shown in Figure S1 and functioned as the working electrode within a two-electrode system, where a Pt rod was employed as the counter electrode. This electrochemical flow-cell was specifically designed to combine electrochemistry with X-ray measurements and was used in numerous previous *in situ* investigations involving NP-AAO.[29,30,48−51] A remotely controlled automated deposition apparatus, consisting of solution reservoirs, solenoid valves, and distribution valve, was used to deliver controlled amounts of electrolyte in the electrochemical cell. Such a system, originally designed for electrochemical atomic layer deposition,[52] was used in this work to exchange Au- and Pd-containing electrolytes.

The deposition apparatus was connected to the two individual reservoirs of Au(III) and Pd(II) electrolyte solutions and to a reservoir of ultrapure $H_2O$. The latter was used to rinse the flow-cell before exchanging the electrolytes to avoid cross-contamination of the system. The electrolyte solutions were freshly prepared before the experiment


https://doi.org/10.1021/acsanm.3c05487
ACS Appl. Nano Mater. 2024, 7, 3861−3872

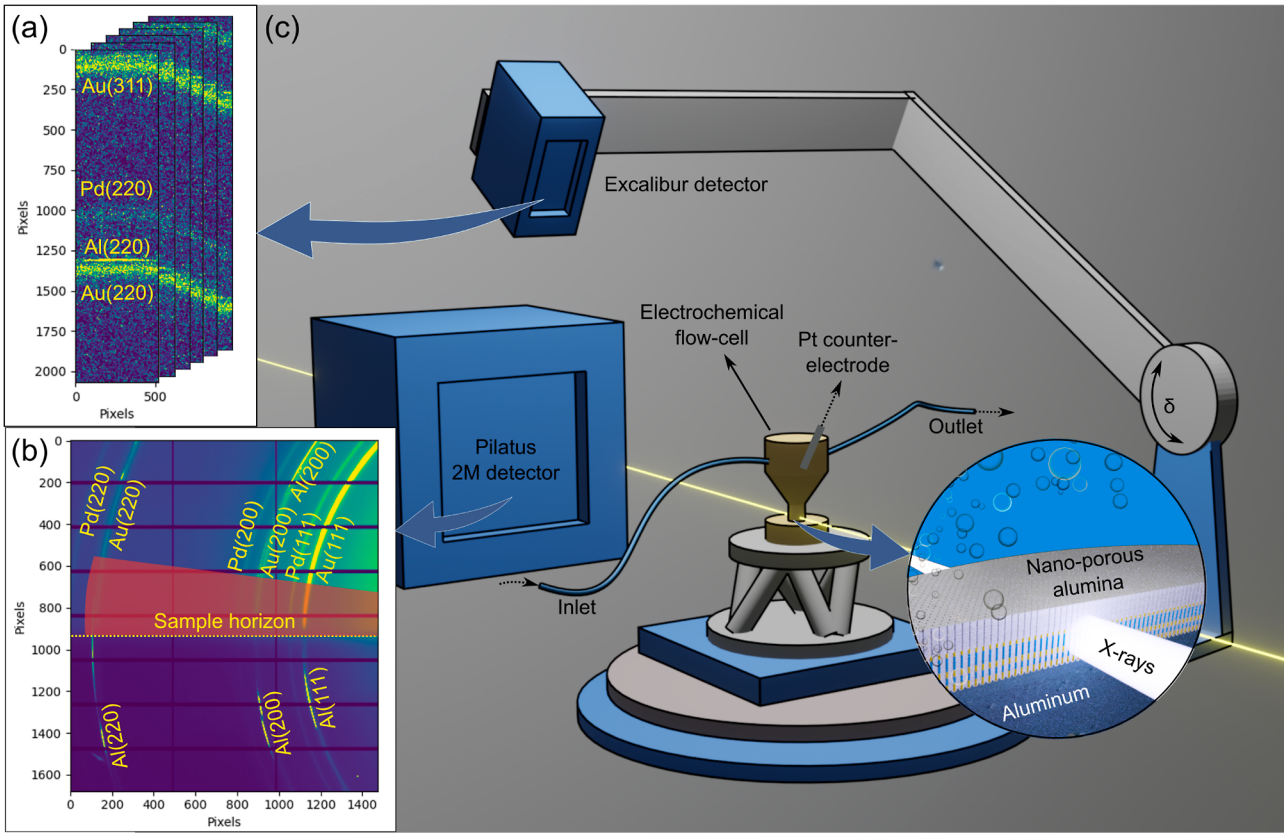


**Figure 2.** Representative stack of detector images acquired by the Excalibur area detector during a $\delta$ scan (a). Representative detector image acquired by the Pilatus 2 M area detector (b). Schematic depiction of the experimental setup: a beam of X-rays impinge the porous alumina template inserted in the electrochemical flow-cell. Powder diffraction rings are detected by two area detectors, which arise from the Au and Pd segments electrodeposited in the template (c).

using ultrapure $H_2O$. The Au(III) electrolyte consisted in a phosphate buffer of neutral pH prepared by gently mixing and stirring diluted $H_3PO_4$ and KOH to a final concentration of 1 and 2 M, respectively, with the addition of 6 mM $KAuCl_4$ and 10 mM $H_2SO_4$. The Pd(II) electrolyte was prepared by dissolving 6 mM $PdCl_2$ in 0.74 M HCl. While stirring, diluted $NH_4OH$ was added in small aliquots to reach a final concentration of 0.81 M. The pH was adjusted to 8.2 by small additions of HCl.

In this work, we employed the pulsed electrodeposition method (PED). A single square-wave of potential with a peak-to-peak amplitude of 20 V and a period of 4 ms, followed by a rest period of 196 ms, was applied to the electrolyte. During the cathodic half-wave, the metal ions are reduced, while during the anodic half-wave, the capacitance of the barrier layer at the pore bottom is discharged. The rest period allowed replenishment of the metal ions in the pores via ion diffusion.[23,43,53] The electrodeposition of gold involves the electrochemical reaction depicted below[54]

$$AuCl_4^- + 3e^- \rightarrow Au^0 + 4Cl^-$$

In contrast, when employing ammonia-based $PdCl_2$ electrolytes, the electrodeposition takes place through the following reaction[55]

$$Pd(NH_3)_4^{2+} + 2e^- \rightarrow Pd^0 + 4NH_3$$

To monitor the current passing through the electrochemical cell, the potential across a 25 Ω shunt resistor in series with the cell was measured using a digital oscilloscope (PicoScope 3000), and the current was derived using Ohm's law. The oscilloscope captured current waveforms with a resolution of 2 ns every 7.5 s. Uniform electrodeposition conditions were maintained for both the PW and BLT templates to enable a systematic comparison.

**XRD Setup.** The *in situ* XRD measurements were performed at beamline I07 (Diamond Light Source, UK)[56] using an X-ray beam with an energy of 19.9 keV and a size of 100 × 300 $\mu$m (vertical × horizontal). The flow-cell was mounted on a (2 + 3)-type surface diffractometer and aligned against the X-ray beam so that the beam would impinge on the template surface at a grazing-incidence angle of 0.5°. In order to study the anisotropy of the system, two detectors were used. An Excalibur area detector composed of Medipix modules with 55 $\mu$m pixel size[57] and mounted on the diffractometer arm was scanned in the vertical plane, rotating the detector arm by $\delta$ (see Figure 2c), in such a way that the scattering vector would be nearly aligned with the direction of growth. In order to capture XRD data with the scattering vector lying on the horizontal plane (i.e., along the direction of pore confinement), a Pilatus 2 M area detector was used (pixel size = 172 $\mu$m).[58] The stacks of images collected with the Excalibur detector scans (such as those in Figure 2a) were processed using angle calculations previously presented,[59] while the Pilatus 2 M images were subject to azimuthal integration using the Python module *PyFAI*,[60] in the azimuthal range of 0−5°, represented by the highlighted areas in Figure 2b. PyFAI enables the transformation of a detector image, or a fraction of it, into a powder diffractogram based upon parameters obtained by processing an XRD pattern of a standard reference material (NIST $LaB_6$). All the detector images were normalized by the intensity of the incoming X-ray beam. In order to avoid radiation damage artifacts, the sample was translated across the beam by ±0.5 mm around the original sample position between consecutive measurements. The schematic in Figure S1a outlines the procedural framework of the *in situ* measurements, while Figure S1b is a schematic of the electrochemical flow-cell. To ensure the integrity of the measurements and prevent any potential beam-induced deposition, the stages involving electrolyte flow and metal electrodeposition were executed with the X-ray shutter closed. Every nanowire segment was deposited in five electrodeposition sequences of 2 min each. After every deposition sequence, the cell was thoroughly rinsed by flowing ultrapure $H_2O$ and the X-ray shutter was


https://doi.org/10.1021/acsanm.3c05487
ACS Appl. Nano Mater. 2024, 7, 3861−3872

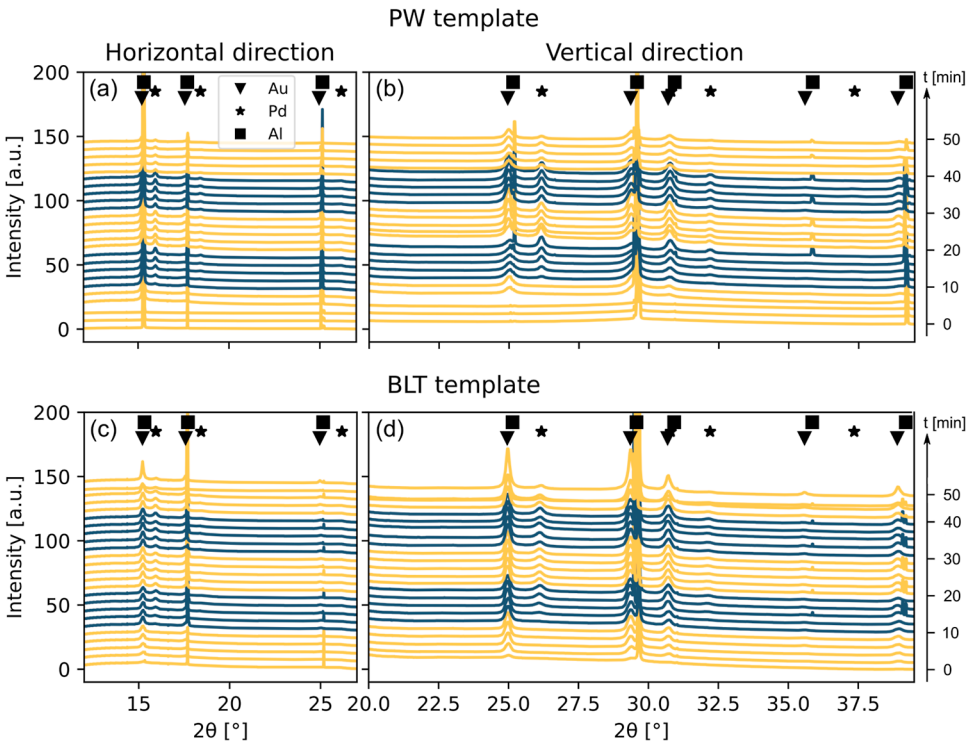


**Figure 3.** X-ray powder diffraction curves obtained during the *in situ* electrodeposition into the PW template (a,b) and in the BLT template (c,d). The curves in (a,c) were acquired with the scattering vector lying in the horizontal plane while those in (b,d) were acquired with the scattering vector nearly aligned with the direction of growth.

opened to initiate the XRD measurement: the Excalibur detector rotated in 20 s fly scans in the $2\theta$ range of 22−58° with an acquisition step of 0.02°, while the Pilatus 2 M detector acquired images with an exposure time of 3 s.

**Electron Microscopy.** The samples of Au−Pd nanowires fabricated in the *in situ* experiments were analyzed by *ex situ* electron microscopy. FIB-SEM analyses were carried out at the Lund Nano Lab using a Nova NanoLab 600 Dual-beam system manufactured by the FEI Company. The purpose of these observations was to visualize the pores and nanowires present within the oxide. To achieve this, a trench was milled into the alumina templates using a focused ion beam of Ga ions. Subsequently, the pores were imaged laterally, at an angle of 52°, capturing the embedded Au−Pd nanowires through the detection of backscattered electrons.

TEM, STEM-EDS, and SAED measurements were carried out at the National Center for High-Resolution Electron Microscopy in Lund (Sweden). For these analyses, the Au−Pd nanowires deposited in the PW template were released in solution by selective dissolution of the NP-AAO template in 1 M KOH at room temperature. Following this, the nanowires were allowed to precipitate by leaving the solution to settle overnight. Subsequently, the mixture underwent repeated and thorough rinsing steps. The first step involved removing the supernatant and replacing it with ultrapure $H_2O$ several times. In the final rinse, ethanol replaced the solvent. To disperse the nanostructures, the solution underwent sonication for 30 min. A total volume of 20 $\mu$L of the solution was then carefully applied to a TEM grid with a holey carbon film. While a significant portion of the ethanol permeated through the TEM grid, a small volume of the solution, which adhered to the TEM grid, was allowed to evaporate. This process leads to a dispersion of nanowires on the holey carbon film. The analysis of the liberated Au−Pd nanowires was conducted with a JEM3000F TEM operating at 300 kV. The analysis of all electron microscopy images was conducted using ImageJ.[61]

## RESULTS AND DISCUSSION

The Au−Pd nanowires were characterized using XRD in steps after the growth of each segment. The dual-area detector configuration was used to study the anisotropy of the system. The data were integrated to reduce the detector images to one-dimensional curves of integral X-ray powder diffraction intensity or simply X-ray powder diffraction curves, which are shown in Figure 3. The data acquired during electrodeposition into the PW template, for the two detector geometries employed (horizontal and vertical, see the Experimental Section) are shown in Figure 3a,b. Similarly, the integrated data obtained from electrodepositing into the BLT template, is reported in Figure 3c,d for the horizontal and vertical direction, respectively. Both experiments were conducted under same conditions of electrodeposition potentials, duration, electrolyte composition, and concentration and have the same time resolution of 2 min. The yellow and the dark cyan lines correspond to electrodeposition sequences of Au and Pd, respectively.

Prior to the electrodeposition start, at time 0, only one fcc phase is observed in diffraction, corresponding to the Al substrate. Note that not all the $(h, k, l)$ Al reflections allowed by fcc crystal symmetry may be present in the diffraction patterns, hence XRPD curves. That is because not all the Al Bragg spots fell under the image integration range due to the strong texturing of the Al substrates (see Figure 2b). Furthermore, some Al reflections observed in a few diffraction patterns may disappear in others because the samples were translated by ±0.5 mm across the X-ray beam between two consecutive measurements to avoid radiation damage. Therefore, some Al grains are in the Bragg condition in one measurement and disappear in the successive one or vice versa.

During our deposition sequence, which involved alternating electrodeposition steps of Au and Pd, distinct phases were


https://doi.org/10.1021/acsanm.3c05487
ACS Appl. Nano Mater. 2024, 7, 3861−3872

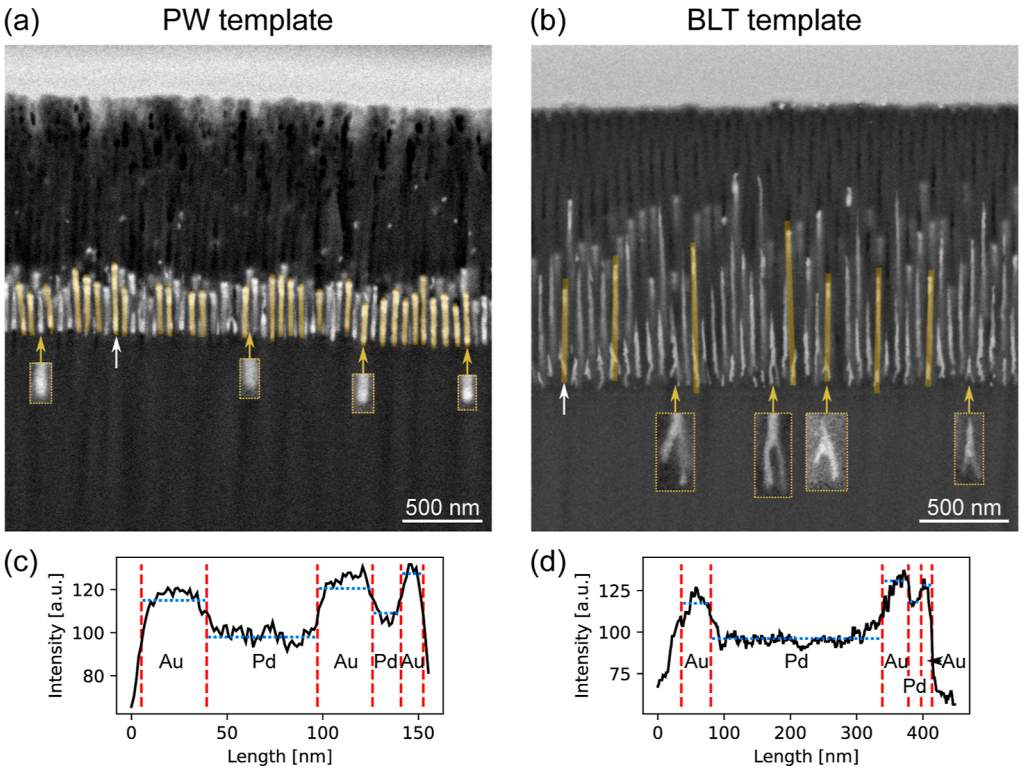


**Figure 4.** FIB-SEM micrographs captured in backscatter electron imaging mode of the two templates studied in this work after electrodeposition: PW (a) and BLT (b). The images reveal the barcode nanowires embedded in the nanoporous template. The arrows point at two representative nanowires whose line profiles are plotted in (c,d), respectively. The line profiles of the highlighted nanowires are reported in the Supporting Information document.

discernible in the XRPD signal. Initially, following a 2 min Au electrodeposition, a clearly identifiable fcc phase emerged, linked to the presence of Au. This signal exhibited a gradual and progressive increase over the following four deposition sequences. After a duration of 10 min, a third distinguishable fcc phase emerged, conclusively identified as Pd. This observation aligns with the deposition history of Pd during that specific time frame. The positions of Au, Al, and Pd Bragg peaks are shown in Figure 3 and their positions, reported in Table S1, were calculated from theoretical bulk values.

The FIB-SEM images in Figure 4 show a cross-sectional view of the templates after the electrodeposition of focus-ion-beam-milled areas in the two templates studied: PW (a) and BLT (b). The backscatter electron imaging mode offered atomic number contrast between Au and Pd that allowed us to identify nanowires with five segments, coherently with the electrodeposition sequences carried out alternating Au with Pd five times. The nanowires that were more clearly imaged and supposedly not damaged by the action of the focused ion beam were highlighted in yellow and their line profiles are reported in the Supporting Information. Two representative profiles, indicated with the white arrow, are reported in Figure 4c,d. The dashed red vertical lines represent the segmental boundaries. The contrast of the Au and Pd segments in the FIB-SEM images was high enough to distinguish segments, and the subdivision of the nanowires was done systematically according to the following steps: (i) a baseline (blue dashed line) was drawn along segments of the same kind, (ii) the difference between the baseline of adjacent segments was calculated, and (iii) the position of half the difference was taken as the boundary of the segment. The regions of higher intensity are attributed to Au, while the ones of lower intensity to Pd, since the backscatter electron signal is proportional to the atomic number.[62]

The template preparation method has an impact on the morphology of the deposited nanowires: while the PW treatment leads to the formation of nanowires with round bottoms, the BLT results in a branched structure of the pores and hence nanowires Figure 4a,b. Since the PW leads to an isotropic etch, the pores have a round-bottom and larger pores compared to the untreated template (46 vs 25 nm[22]). On the other hand, the BLT leads to branching of the pores since the pore density is inversely proportional to the anodizing potential,[63,64] which is slowly decreased immediately after the second anodization (see the Experimental Section). Although BLT was used in this work as a solution to enable electrodeposition in the template, it is also an established method to fabricate hierarchical nanoarchitectures.[65]

Although each electrodeposition sequence was conducted using the same conditions of applied potential, electrolyte composition, and duration, we observed that segments of the same element become progressively shorter. This observation is based on Z-contrast measurements of segmental lengths extracted from the line profiles of 23 nanowires (16 and 7 in the PW and the BLT template, respectively), which are shown in the Supporting Information. Two examples of such line profiles, one for each template, are shown in Figure 4c,d. The shortening of the segments could be due to an increase in the resistivity of the system over time. In fact, Sauer et al.[53] (2002) observed an increase in the peak-to-peak potential during the current-limited Ag electrodeposition in NP-AAO, revealing a similar overall resistivity increase. The authors attributed this phenomenon to a


https://doi.org/10.1021/acsanm.3c05487
ACS Appl. Nano Mater. 2024, 7, 3861−3872

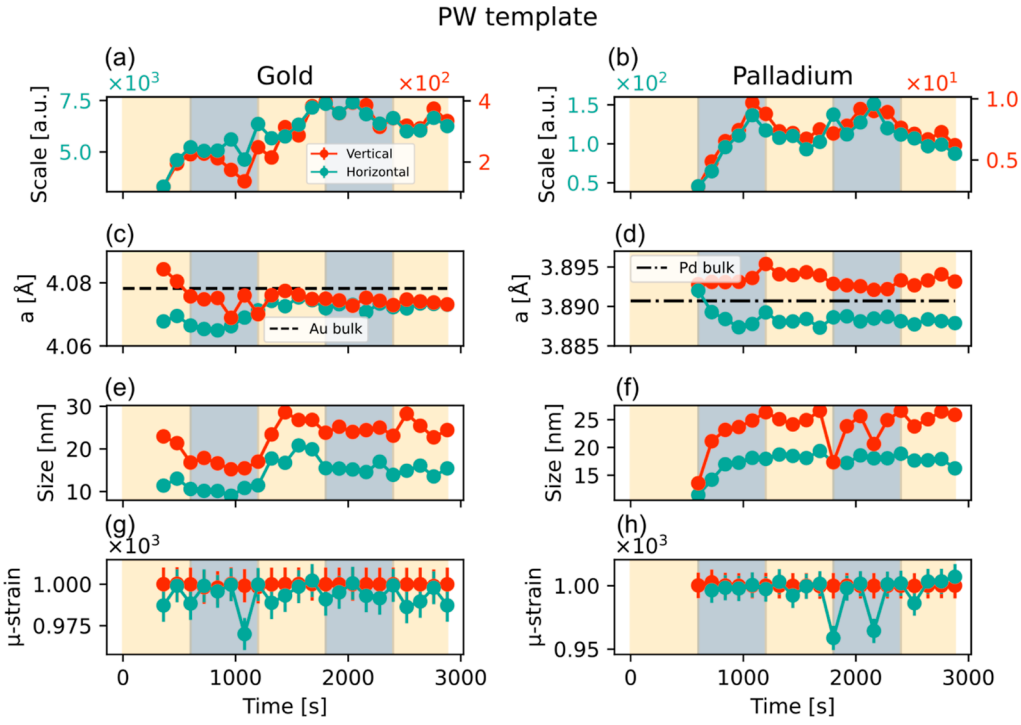


**Figure 5.** Rietveld refinement results of the data acquired during *in situ* electrodeposition in the PW template: scale factors (a,b), lattice parameters (c,d), crystallite size (e,f), and microstrain (g,h).

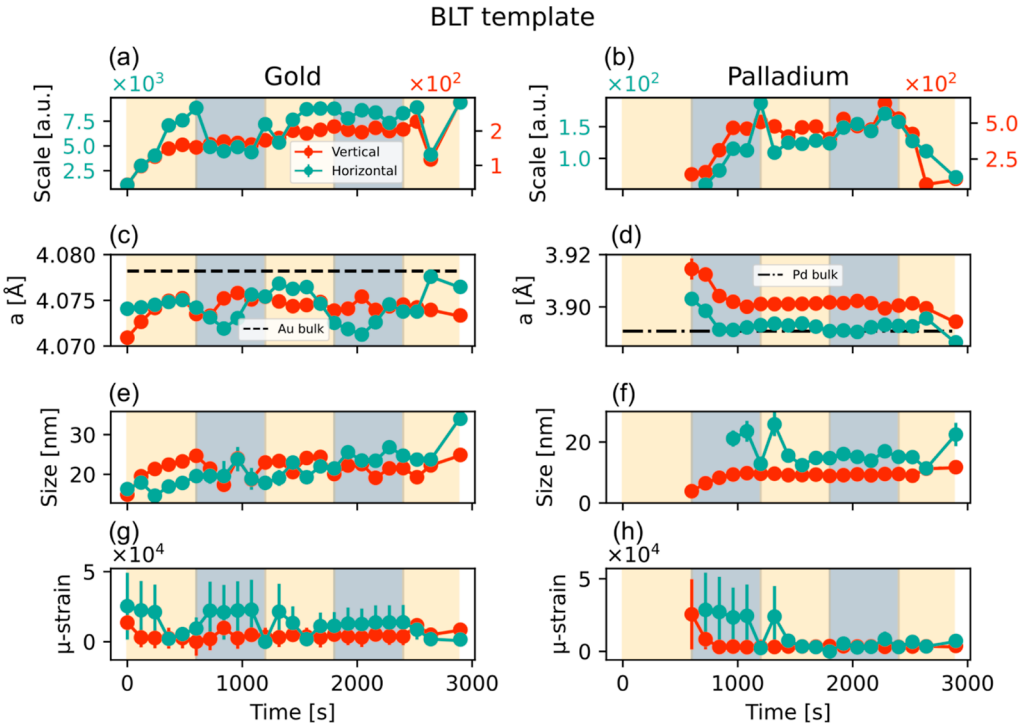


**Figure 6.** Rietveld refinement results of the data acquired during *in situ* electrodeposition in the BLT template: scale factors (a,b), lattice parameters (c,d), crystallite size (e,f), and microstrain (g,h).

depletion of metal ions in the pores as the deposited metal progressively replaces the electrolyte.

The presence of the two fcc phases due to Au and Pd observed in the XRD data is confirmed by TEM investigations. Figure S4a shows some nanowires which were released from the PW template. The ones in the circled area gave rise to the SAED pattern in Figure S4b, where two sets of fcc phases were identified as Au and Pd.

In order to extract quantitative information from the *in situ* XRD data, the patterns from both detector geometries, shown earlier in Figure 3, were fed to a Rietveld refinement algorithm using the software *GSAS-II*[66] to extract the intensity scale factors, lattice parameters, crystallite size, and microstrain from



https://doi.org/10.1021/acsanm.3c05487
ACS Appl. Nano Mater. 2024, 7, 3861−3872

each phase. The results of the Rietveld refinement are summarized in Figures 5 and 6, where the plot background colors yellow and cyan represent electrodeposition sequences of Au or Pd, respectively. For both horizontal and vertical orientations and for both samples, the intensity scale factors of Au and Pd increase over time with the exception of the Pd signal in the PW template (Figure 5b). Here, the Pd intensity decreases in the stages where the Au is deposited due to the attenuation of the diffracted X-rays by the overlying Au segment. Our measurements demonstrate the absence of the preferred crystallographic orientations for both Pd and Au segments. This is reflected in the homogeneity of diffraction intensity along the powder diffraction rings and leads to the similar increase in the calculated scale factors.

The lattice parameters of Au and Pd in the PW sample are shown in Figure 5c,d. The lattice parameter of Au is larger in the vertical direction than in the horizontal one in the first stages of electrodeposition; subsequently, both lattice parameters tend to the same value of approximately $4.074 \pm 0.002$ Å. The Pd lattice parameter shows the opposite behavior: it is nearly isotropic in the very beginning of the first Pd deposition stage and quickly becomes more anisotropic as the deposition progresses. The divergence of Pd lattice parameter in nanowires along and perpendicular to growth direction has been observed in previous research,[23] and it is attributed to the growth of the nanostructures under confinement. In a simplified model where a nanowire is described by cylinder, a hoop stress causes a strain along the nanowire radius which in turn causes an elongation along the height due to the Poisson effect.[28,67]

In the BLT template, the evolution of the Pd lattice parameter shows a similar trend as in the case of the PW template (Figure 6d), while the Au lattice parameter is nearly constant in the vertical direction and oscillates in the horizontal direction in phase with the exchange of electrodeposited metal. This shows that the electrodeposition of a Pd segment strongly influences the lattice parameter of the pre-existing Au segment and vice versa. One possible reason for this variation is the alloying of Au with Pd. In fact, bulk Au has a larger lattice parameter than Pd (4.078 vs 3.890 Å[68,69]) and the presence of Pd atoms in the Au lattice would lead to a decrease of the lattice parameter, as predicted by Vegard's law.[70] Our STEM-EDS analysis conducted on a single barcode nanowire, displayed in Figure 7, showed traces of Pd in proximity of the nanowire bottom, i.e., the first Au segment deposited. This could be an evidence of interdiffusion or formation of interfaces such as core−shell or Au side-by-side with Pd. Similar evidence was not found among the other segments of the nanowire. Nonetheless, interdiffusion of the two elements at the metal/metal interface on a subnanometer scale cannot be excluded. Since segments of different kinds are quite distinguishable on the only evidence of possible alloying is limited to the first segment deposited, we can attribute the lattice parameter variations observed in the *in situ* XRD data to strain caused by nanoconfinement and interfacial effects.

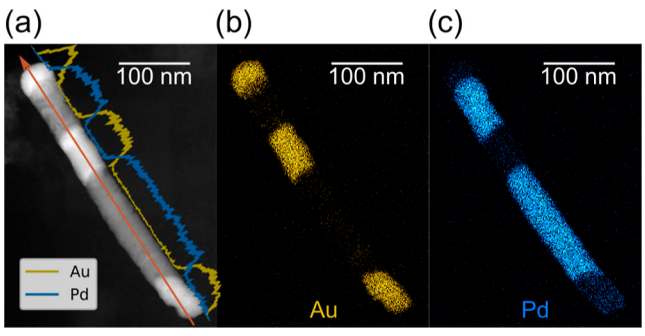


**Figure 7.** Dark-field STEM image of a single nanowire (a) and STEM-EDS maps of Au (b) and Pd (c).

High-resolution (HR) TEM and STEM-EDS images of an interface between Au and Pd segments are shown in Figure 8. The STEM-EDS revealed that the bottom half of the nanowire in (d) is Pd, while the upper half is Au. The line profile of the two elements shown in (a) suggests a graded interface, rather than an abrupt junction. We observe that in most cases, the interface between Pd and Au segments is of irregular shape and not well-defined. Therefore, it is not possible to determine accurately whether or not there is a significant interdiffusion of elements between the adjacent segments. An important observation stems from the analysis of the fast Fourier transforms (FFTs) of the HR-TEM micrographs of Au and Pd segments, shown in Figure 8e,f and highlighted in Figure 8d, with yellow squares. The measured polar coordinates $(r, \theta)$ of the vectors are $(2.72 \pm 0.07$ Å$^{-1}$, $107 \pm 0.1°)$ for Au and $(2.87 \pm 0.07$ Å$^{-1}$, $107 \pm 0.1°)$ for Pd. The $r$ values acquired are consistent with the 2.31 and 2.19 Å planar spacings found in Au(111) and Pd(111), respectively. The lattice parameters for these two materials can be determined from the following spacings: $4.00 \pm 0.1$ Å for Au and $3.79 \pm 0.09$ Å for Pd. The fact that the orientation of both vectors is 107° evidences that, despite the graded segment interface and the large lattice mismatch, the two segments have same crystallographic orientation as if the growth was epitaxial.

With GSAS-II, the crystallite size and the microstrain were derived from the Lorentzian and the Gaussian components of the XRD peak broadening, respectively. The crystallite size of the nanowires in the PW sample is greater in the direction of confinement than in the direction of growth Figure 5e,f. This anisotropy has been observed in previous studies,[22,30] and it is ascribed to the growth confinement inside the long narrow pores. Interestingly, such behavior is not as evident in the case of the BLT template Figure 6e,f.

The microstrain of the nanowires in the PW sample is constant throughout the electrodeposition for both Au and Pd Figure 5g,h, while it shows some variations in the BLT sample Figure 6g,h. Here, the Au microstrain is high at the beginning of the electrodeposition, and it decreases after 8 min. This could be attributed to the filling of the branches at the pore bottom and to the nucleation of nanoparticles with high density of defects and dislocations, which cause a significant strain. In fact, by relating the Gaussian XRD peak widths to the dislocation density with the model presented by Dunn and Kogh,[71] we found a dislocation density of $\approx 1.27 \times 10^{-9}$ cm$^{-2}$. A second increase in the Au microstrain is observed during the electrodeposition of Pd. We attribute this effect to the large lattice mismatch between the two metals (≈4.6%), as codeposition of Au and Pd is known to cause stress build-up and formation of defects in Au−Pd films.[72,73] We did not observe this effect during the electrodeposition of the second Pd segment ($1800 \text{ s} < t < 2400$ s), probably due to the averaging of the Pd signal between the newly formed Pd and the already deposited Pd segments ($600 \text{ s} < t < 1200$ s).

This reasoning can be extended to all the results shown in Figures 5 and 6 for $t > 1200$ s. For instance, the lattice parameter of the second Au segment is averaged with the first one and this trend continues across subsequent segments of the same metal.


https://doi.org/10.1021/acsanm.3c05487
ACS Appl. Nano Mater. 2024, 7, 3861−3872

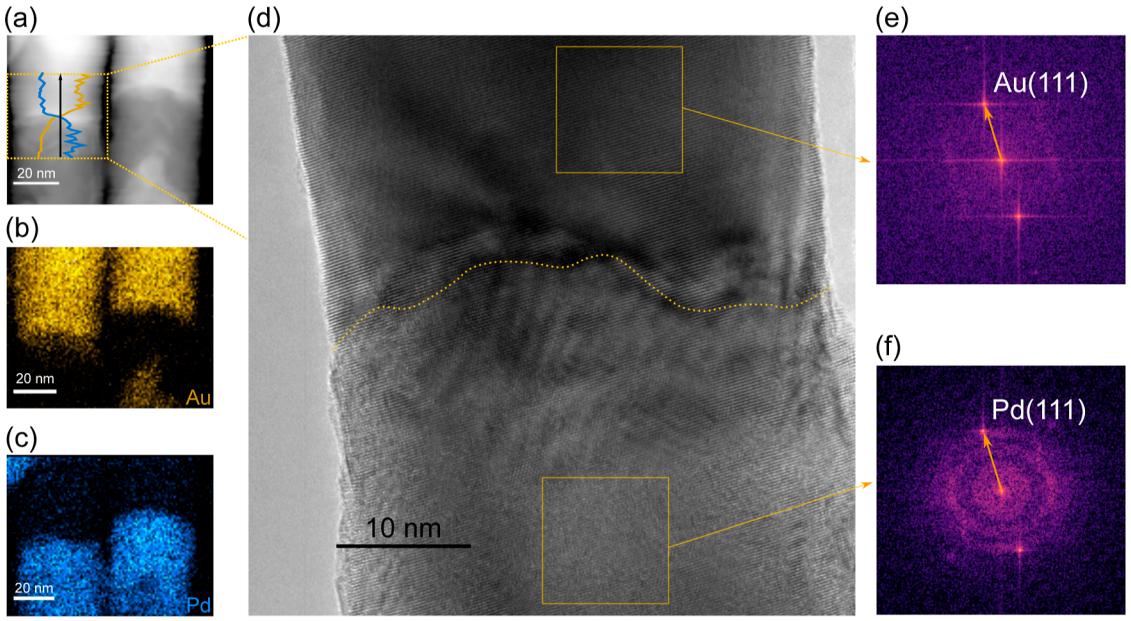


**Figure 8.** Dark-field STEM image of two adjacent nanowires (a). STEM-EDS maps of Au (b) and Pd (c). HRTEM of the nanowire in the boxed area in (a). FFTs of the boxed areas in (d) Au (e) and Pd (f).

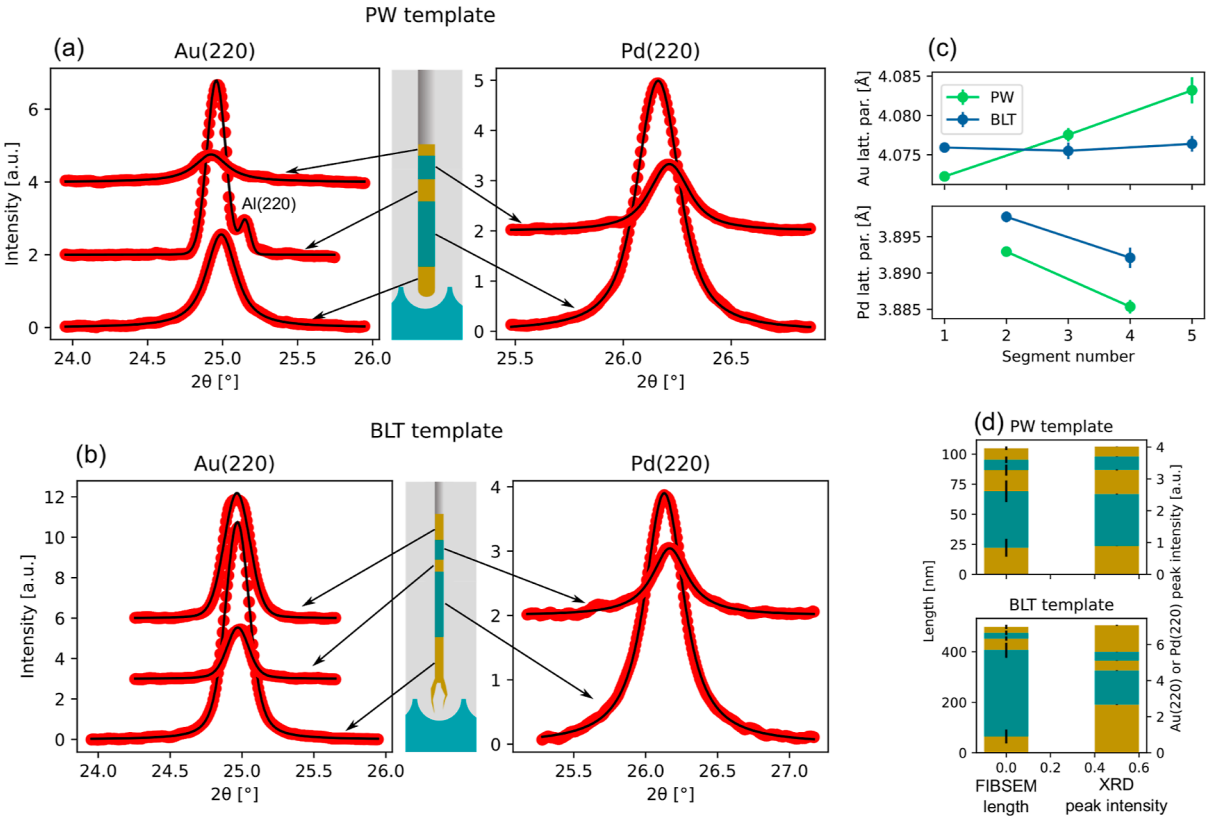


**Figure 9.** Differential XRD peaks arising from the Au(220) and Pd(220) reflections for the PW (a) and BLT (b) templates. Lattice parameters derived by the peak positions of the fits (c). Bar plots comparing the FIB-SEM-derived segmental lengths and the peak amplitudes resulting from the fits in (a,b).

Therefore, in order to obtain the structural information from a single ensemble of segments, we calculated the differential XRD patterns taken at the end of a deposition sequence for adjacent segments. This operation can be summarized by the following equation

$$y_i^{\mathrm{D}} = y(t_i) - y(t_{i-1}) \tag{1}$$

where $y_i^{\mathrm{D}}$ is the calculated differential XRD patterns and $y(t_i)$ represents an XRD pattern at the time $t_i$, with $t_i = i \times 600$ s and $i$ ranging from 1 to 5.



https://doi.org/10.1021/acsanm.3c05487
ACS Appl. Nano Mater. 2024, 7, 3861−3872

The results of this differential approach for patterns acquired in the vertical direction are shown in Figure 9 for the PW (a) and BLT (b) templates. The Au(220) and Pd(220) peaks were fitted with Voigt functions using the Python *lmfit* module.[74] Lmfit is a curve-fitting tool that uses nonlinear least-square minimization. The peak positions from the fits were used to calculate the lattice parameters, reported in Figure 9,c as a function of the segment number. The Au lattice parameter is constant for the BLT sample, and it increases for the PW sample, evidence of the Poisson-effect-induced elongation described earlier. Remarkably, the Pd lattice parameter decreases for both templates.

The amplitudes of the XRD peaks in Figure 9a,b were reported in the bar plot in (d), alongside with the FIB-SEM-derived segmental lengths, calculated averaging all the lengths measured, as shown in Figures S2 and S3. In the case of the PW template, there is a good agreement between the XRD peak amplitude and the segmental lengths. While the statistical population of FIB-SEM-derived lengths is based on the observation of 16 nanowires, the XRD intensities are averaged over $4.9 \times 10^8$ nanowires (this number was calculated by multiplying the pore density by the area of the beam footprint on the template). The fact that a randomly selected area for the FIB milling contains nanowires that can represent such a highly statistical information shows how well-reproducible and uniform the nanowires are in each pore. On the other hand, there is no such agreement between the FIB-SEM lengths and all the XRD amplitudes for the BLT template, meaning that the statistical population of lengths measured with electron microscopy is not representative of the entire sample. Similar length heterogeneity was observed in the case of the Au nanorods synthesized in previous research in BLT templates, where unhomogeneous barrier layer thicknesses lead to a high standard deviation of rod length.[22]

The average length of the nanowires in the PW template is $106 \pm 15$ nm, and the nanowires in the BLT template have an average length of $493 \pm 63$ nm. Their respective segmental lengths are reported numerically in Table S2 and as histograms in Figure 9d.

Despite the heterogeneous lengths, the analysis of FIBSEM-derived segment lengths and XRD peak areas shown in Figure 9d revealed that in both templates, segment 4 is smaller than segment 2. This evidence can explain the decrease of the Pd lattice parameter discussed earlier Figure 9c as the bond-order-length-strength model predicts a contraction of the crystal lattice inversely proportional to the nanoparticle size.[75,76]

In the case of the PW template, the agreement between the FIBSEM-derived segment lengths and the XRD peak areas suggests that the electrode position of Au−Pd nanowires, combined with the differential *in situ* XRD approach that we presented, is an ideal tool to grow barcode nanowires with controlled length and lattice parameters of the segments. In principle, the length of segments could be controlled by integrating the electrochemical currents over time, in order to obtain how much charge has passed through the working electrode and relating it to the amount of mass deposited. However, the current data shown in Figure S5 shows that this is not the case. This plot reports the current averaged between 1 and 2 ms after the beginning of each measured current pulse, as shown in the Figure inset, in a similar way to how normal pulse voltammetry data is processed.[77] Although it has been shown earlier that the segments become shorter with deposition time (see Figure 4), in Figure S5, we see a current increase. In the assumption that the electrodeposition efficiency is 100%, this would mean that the barcode segments would become longer with time. Such conflictual information can be explained by the fact that both Au and Pd are efficient catalysts for the hydrogen evolution reaction. As the nanowires grow, part of the cathodic current density increasingly contributes to the production of hydrogen, leading to a progressive decrease in the electrodeposition efficiency.

## CONCLUSIONS

In this study, we successfully demonstrated a controlled fabrication approach for producing Au−Pd barcode nanowires with tunable segments and lattice parameters. Through a comprehensive investigation using *in situ* XRD, FIB-SEM, and TEM, we have gained valuable insights into the influence of template preparation methods on the growth and structural characteristics of these nanostructures.

Our results highlight the significance of template treatments, such as PW and BLT, in tailoring nanowire growth. The sequential deposition of Au and Pd segments with observed lattice parameter variations underscores the complexity of alloying effects and strain modulation within confined nanoscale architecture.

The uniform lengths of nanowires achieved in the pore-widened templates signify a controlled growth process, opening avenues for reproducible fabrication. The TEM analysis not only confirms the distinct yet contiguous nature of Au and Pd segments but also highlights the preservation of the crystallographic orientation at the boundaries. While we provide valuable insights into our successful fabrication method, the direct consequences on interdiffusion require further investigation.

The combination of advanced characterization techniques has allowed us to comprehend the intricate dynamics involved in the electrodeposition process and the resulting nanostructure formation. This work not only contributes to the fundamental understanding of multimetallic nanostructure synthesis but also holds promise for various practical applications, particularly in the realm of catalysis.

Looking forward, the insights gained from this study could serve as a foundation for further explorations into designing and fabricating intricate nanoarchitecture with tailored properties. The ability to control and manipulate nanowire segments at the atomic scale offers exciting possibilities for engineering novel materials with enhanced functionalities, advancing both the scientific understanding and technological innovation.

## ASSOCIATED CONTENT

### Supporting Information

The Supporting Information is available free of charge at https://pubs.acs.org/doi/10.1021/acsanm.3c05487.

Comprehensive FIB-SEM images used for the barcode segment length evaluation; TEM micrograph with SAED; $2\theta_B$ diffraction angles of bulk Au, Pd, and Al; and plot of the cathodic electrochemical currents (PDF)

## AUTHOR INFORMATION

### Corresponding Author

**Giuseppe Abbondanza** − *Department of Physics, Chalmers University of Technology, 412 96 Gothenburg, Sweden;* orcid.org/0000-0002-0680-5454; Email: giuseppe.abbondanza@chalmers.se



https://doi.org/10.1021/acsanm.3c05487
*ACS Appl. Nano Mater.* 2024, 7, 3861−3872

### Authors

**Andrea Grespi** − *Division of Synchrotron Radiation Research, Lund University, 221 00 Lund, Sweden;* orcid.org/0000-0003-3132-4318

**Alfred Larsson** − *Division of Synchrotron Radiation Research, Lund University, 221 00 Lund, Sweden;* orcid.org/0000-0002-8932-8381

**Crispin Hetherington** − *nCHREM, Lund University, 221 00 Lund, Sweden;* orcid.org/0000-0002-4905-9965

**Matthew Snelgrove** − *Diamond Light Source, OX11 0DE Didcot, U.K.*

**Francesco Carlá** − *Diamond Light Source, OX11 0DE Didcot, U.K.*

**Nikolay Vinogradov** − *MAX IV Laboratory, Lund University, 224 84 Lund, Sweden;* orcid.org/0000-0002-1477-853X

**Roberto Felici** − *CNR-SPIN, I-00133 Rome, Italy;* orcid.org/0000-0001-9897-5866

**Edvin Lundgren** − *Division of Synchrotron Radiation Research, Lund University, 22100 Lund, Sweden;* orcid.org/0000-0002-3692-6142

Complete contact information is available at: https://pubs.acs.org/10.1021/acsanm.3c05487


### Notes

The authors declare no competing financial interest.

## ■ ACKNOWLEDGMENTS

This work was carried out with the support of Diamond Light Source, beamline I07 (proposal SI30356-1). This work was financially supported by the Swedish Research Council through the Röntgen-Ångström-Cluster "In situ High-Energy XRD from Electrochemical Interfaces (HEXCHEM)" (Project no. 2015-06092) and project grant "Understanding and Functionalization of Nano Porous Anodic Oxides" (Project no. 2018-03434) by the Swedish research council. The Swedish Research Council and the Swedish Foundation for Strategic Research are acknowledged for access to ARTEMI, the Swedish National Infrastructure in Advanced Electron Microscopy (grant no. 2021-00171 and no. RIF21-0026). We acknowledge financial support by NanoLund.

## ■ REFERENCES


(1) Zhuo, X.; Zhu, X.; Li, Q.; Yang, Z.; Wang, J. Gold Nanobipyramid-Directed Growth of Length-Variable Silver Nanorods with Multipolar Plasmon Resonances. *ACS Nano* **2015**, *9*, 7523−7535.

(2) Yang, Y.; Wang, W.; Li, X.; Chen, W.; Fan, N.; Zou, C.; Chen, X.; Xu, X.; Zhang, L.; Huang, S. Controlled Growth of Ag/Au Bimetallic Nanorods through Kinetics Control. *Chem. Mater.* **2013**, *25*, 34−41.

(3) Seo, D.; Yoo, C. I.; Jung, J.; Song, H. Ag-Au-Ag Heterometallic Nanorods Formed through Directed Anisotropic Growth. *J. Am. Chem. Soc.* **2008**, *130*, 2940−2941.

(4) Rodal-Cedeira, S.; Montes-García, V.; Polavarapu, L.; Solís, D. M.; Heidari, H.; La Porta, A.; Angiola, M.; Martucci, A.; Taboada, J. M.; Obelleiro, F.; Bals, S.; Pérez-Juste, J.; Pastoriza-Santos, I. Plasmonic Au@Pd Nanorods with Boosted Refractive Index Susceptibility and SERS Efficiency: A Multifunctional Platform for Hydrogen Sensing and Monitoring of Catalytic Reactions. *Chem. Mater.* **2016**, *28*, 9169−9180.

(5) Kline, T. R.; Tian, M.; Wang, J.; Sen, A.; Chan, M. W. H.; Mallouk, T. E. Template-Grown Metal Nanowires. *Inorg. Chem.* **2006**, *45*, 7555−7565.

(6) Zhu, X.; Guo, Q.; Sun, Y.; Chen, S.; Wang, J.-Q.; Wu, M.; Fu, W.; Tang, Y.; Duan, X.; Chen, D.; Wan, Y. Optimising surface d charge of AuPd nanoalloy catalysts for enhanced catalytic activity. *Nat. Commun.* **2019**, *10*, 1428.

(7) Xu, C.-Q.; Lee, M.-S.; Wang, Y.-G.; Cantu, D. C.; Li, J.; Glezakou, V.-A.; Rousseau, R. Structural Rearrangement of Au−Pd Nanoparticles under Reaction Conditions: An ab Initio Molecular Dynamics Study. *ACS Nano* **2017**, *11*, 1649−1658.

(8) Zhang, X.; Sun, Z.; Jin, R.; Zhu, C.; Zhao, C.; Lin, Y.; Guan, Q.; Cao, L.; Wang, H.; Li, S.; Yu, H.; Liu, X.; Wang, L.; Wei, S.; Li, W.-X.; Lu, J. Conjugated dual size effect of core-shell particles synergizes bimetallic catalysis. *Nat. Commun.* **2023**, *14*, 530.

(9) Tedsree, K.; Li, T.; Jones, S.; Chan, C. W. A.; Yu, K. M. K.; Bagot, P. A. J.; Marquis, E. A.; Smith, G. D. W.; Tsang, S. C. E. Hydrogen production from formic acid decomposition at room temperature using a Ag−Pd core−shell nanocatalyst. *Nat. Nanotechnol.* **2011**, *6*, 302−307.

(10) Lee, W.; Scholz, R.; Nielsch, K.; Gösele, U. A Template-Based Electrochemical Method for the Synthesis of Multisegmented Metallic Nanotubes. *Angew. Chem., Int. Ed.* **2005**, *44*, 6050−6054.

(11) Samardak, A. Y.; Jeon, Y. S.; Samardak, V. Y.; Kozlov, A. G.; Rogachev, K. A.; Ognev, A. V.; Jeong, E.; Kim, G. W.; Ko, M. J.; Samardak, A. S.; Kim, Y. K. Interwire and Intrawire Magnetostatic Interactions in Fe-Au Barcode Nanowires with Alternating Ferromagnetically Strong and Weak Segments. *Small* **2022**, *18*, 2203555.

(12) Wang, J. Barcoded metal nanowires. *J. Mater. Chem.* **2008**, *18*, 4017−4020.

(13) Susano, M.; Proenca, M. P.; Moraes, S.; Sousa, C. T.; Araújo, J. P. Tuning the magnetic properties of multisegmented Ni/Cu electrodeposited nanowires with controllable Ni lengths. *Nanotechnology* **2016**, *27*, 335301.

(14) Xu, L.; Wang, K.; Jiang, B.; Chen, W.; Liu, F.; Hao, H.; Zou, C.; Yang, Y.; Huang, S. Competitive Effect in The Growth of Pd−Au−Pd Segmental Nanorods. *Chem. Mater.* **2016**, *28*, 7394−7403.

(15) Gilroy, K. D.; Hughes, R. A.; Neretina, S. Kinetically Controlled Nucleation of Silver on Surfactant-Free Gold Seeds. *J. Am. Chem. Soc.* **2014**, *136*, 15337−15345.

(16) Wang, Z.; Chen, Z.; Zhang, H.; Zhang, Z.; Wu, H.; Jin, M.; Wu, C.; Yang, D.; Yin, Y. Lattice-Mismatch-Induced Twinning for Seeded Growth of Anisotropic Nanostructures. *ACS Nano* **2015**, *9*, 3307−3313.

(17) Niu, G.; Liu, F.; Yang, Y.; Fu, Y.; Wang, W. Synthesis of pentafold twinned Pd-Au-Pd segmental nanorods for in situ monitoring catalytic reaction. *Colloids Surf., A* **2020**, *607*, 125490.

(18) Jung, J.; Seo, D.; Park, G.; Ryu, S.; Song, H. Ag-Au-Ag Heterometal Nanowires: Synthesis, Diameter Control, and Dual Transversal Modes with Diameter Dependency. *J. Phys. Chem. C* **2010**, *114*, 12529−12534.

(19) Niu, Z.; Li, Y. Removal and Utilization of Capping Agents in Nanocatalysis. *Chem. Mater.* **2014**, *26*, 72−83.

(20) Seo, D.; Song, H. Asymmetric Hollow Nanorod Formation through a Partial Galvanic Replacement Reaction. *J. Am. Chem. Soc.* **2009**, *131*, 18210−18211.

(21) Xiao, J.; Qi, L. Surfactant-assisted, shape-controlled synthesis of gold nanocrystals. *Nanoscale* **2011**, *3*, 1383−1396.

(22) Abbondanza, G.; Larsson, A.; Linpé, W.; Hetherington, C.; Carlá, F.; Lundgren, E.; Harlow, G. S. Templated electrodeposition as a scalable and surfactant-free approach to the synthesis of Au nanoparticles with tunable aspect ratios. *Nanoscale Adv.* **2022**, *4*, 2452−2467.

(23) Larsson, A.; Abbondanza, G.; Linpé, W.; Carlà, F.; Mousley, P.; Hetherington, C.; Lundgren, E.; Harlow, G. S. Electrochemical Fabrication and Characterization of Palladium Nanowires in Nanoporous Alumina Templates. *J. Electrochem. Soc.* **2020**, *167*, 122514.

(24) Lee, J. H.; Wu, J. H.; Liu, H. L.; Cho, J. U.; Cho, M. K.; An, B. H.; Min, J. H.; Noh, S. J.; Kim, Y. K. Iron−gold barcode nanowires. *Angew. Chem.* **2007**, *119*, 3737−3741.

(25) Ramulu, T.; Venu, R.; Anandakumar, S.; Rani, V. S.; Yoon, S.; Kim, C. Structure, growth and magnetic property of hard magnetic CoPtP nanowires synthesized by electrochemical deposition. *Thin Solid Films* **2012**, *520*, 5508−5511.

(26) Zhang, L.; Xie, Z.; Gong, J. Shape-controlled synthesis of Au−Pd bimetallic nanocrystals for catalytic applications. *Chem. Soc. Rev.* **2016**, *45*, 3916−3934.

(27) Zhong, M.; Xu, Y.; Li, J.; Ge, Z.-X.; Jia, C.; Chen, Y.; Deng, P.; Tian, X. Engineering PdAu Nanowires for Highly Efficient Direct Methane Conversion to Methanol under Mild Conditions. *J. Phys. Chem. C* **2021**, *125*, 12713−12720.
(28) Shin, H. S.; Yu, J.; Song, J. Y.; Park, H. M. Size dependence of lattice deformation induced by growth stress in Sn nanowires. *Appl. Phys. Lett.* **2009**, *94*, 011906.
(29) Larsson, A.; Abbondanza, G.; Rämisch, L.; Linpé, W.; Novikov, D. V.; Lundgren, E.; Harlow, G. S. In situ scanning x-ray diffraction reveals strain variations in electrochemically grown nanowires. *J. Phys. D: Appl. Phys.* **2021**, *54*, 235301.
(30) Abbondanza, G.; Grespi, A.; Larsson, A.; Glatthaar, L.; Weber, T.; Blankenburg, M.; Hegedüs, Z.; Lienert, U.; Over, H.; Lundgren, E. Anisotropic strain variations during the confined growth of Au nanowires. *Appl. Phys. Lett.* **2023**, *122*, 123101.
(31) Li, Y.; Sun, Y.; Qin, Y.; Zhang, W.; Wang, L.; Luo, M.; Yang, H.; Guo, S. Recent Advances on Water-Splitting Electrocatalysis Mediated by Noble-Metal-Based Nanostructured Materials. *Adv. Energy Mater.* **2020**, *10*, 1903120.
(32) Zhang, H.; Jin, X.; Lee, J.-M.; Wang, X. Tailoring of Active Sites from Single to Dual Atom Sites for Highly Efficient Electrocatalysis. *ACS Nano* **2022**, *16*, 17572−17592.
(33) Hou, Z.; Cui, C.; Li, Y.; Gao, Y.; Zhu, D.; Gu, Y.; Pan, G.; Zhu, Y.; Zhang, T. Lattice-Strain Engineering for Heterogenous Electrocatalytic Oxygen Evolution Reaction. *Adv. Mater.* **2023**, *35*, 2209876.
(34) Xia, Z.; Guo, S. Strain engineering of metal-based nanomaterials for energy electrocatalysis. *Chem. Soc. Rev.* **2019**, *48*, 3265−3278.
(35) Yasin, G.; Ibrahim, S.; Ajmal, S.; Ibraheem, S.; Ali, S.; Nadda, A. K.; Zhang, G.; Kaur, J.; Maiyalagan, T.; Gupta, R. K.; Kumar, A. Tailoring of electrocatalyst interactions at interfacial level to benchmark the oxygen reduction reaction. *Coord. Chem. Rev.* **2022**, *469*, 214669.
(36) Nath, N.; Chakroborty, S.; Pal, K.; Barik, A.; Priyadarsini Mishra, N.; Kralj, S. Recent Advances in Plasmonic Enhanced Nanocatalyst for Oxidation of Alcohol. *Top. Catal.* **2023**.
(37) Zhao, X.; Chang, Y.; Chen, W.-J.; Wu, Q.; Pan, X.; Chen, K.; Weng, B. Recent Progress in Pd-Based Nanocatalysts for Selective Hydrogenation. *ACS Omega* **2022**, *7*, 17−31.
(38) Duan, H.; Zeng, Y.; Yao, X.; Xing, P.; Liu, J.; Zhao, Y. Tuning Synergistic Effect of Au−Pd Bimetallic Nanocatalyst for Aerobic Oxidative Carbonylation of Amines. *Chem. Mater.* **2017**, *29*, 3671−3677.
(39) Ma, T.; Liang, F. Au−Pd Nanostars with Low Pd Content: Controllable Preparation and Remarkable Performance in Catalysis. *J. Phys. Chem. C* **2020**, *124*, 7812−7822.
(40) Liu, R.; Chen, H.-m.; Fang, L.-p.; Xu, C.; He, Z.; Lai, Y.; Zhao, H.; Bekana, D.; Liu, J.-f. Au@Pd Bimetallic Nanocatalyst for Carbon−Halogen Bond Cleavage: An Old Story with New Insight into How the Activity of Pd is Influenced by Au. *Environ. Sci. Technol.* **2018**, *52*, 4244−4255.
(41) Demirok, U. K.; Burdick, J.; Wang, J. Orthogonal Multi-Readout Identification of Alloy Nanowire Barcodes. *J. Am. Chem. Soc.* **2009**, *131*, 22−23.
(42) Yu, X.; Zhang, H.; Yu, J. Luminescence anti-counterfeiting: From elementary to advanced. *Aggregate* **2021**, *2*, 20−34.
(43) Nielsch, K.; Müller, F.; Li, A.-P.; Gösele, U. Uniform Nickel Deposition into Ordered Alumina Pores by Pulsed Electrodeposition. *Adv. Mater.* **2000**, *12*, 582−586.
(44) Cao, X.; Gu, L.; Hu, S.; Mukhtar, A.; Wu, K. Fe/Mn Multilayer Nanowires as High-Performance T1-T2 Dual Modal MRI Contrast Agents. *Materials* **2021**, *14*, 2238.
(45) Jessensky, O.; Müller, F.; Gösele, U. Self-organized formation of hexagonal pore arrays in anodic alumina. *Appl. Phys. Lett.* **1998**, *72*, 1173−1175.
(46) Masuda, H.; Yada, K.; Osaka, A. Self-Ordering of Cell Configuration of Anodic Porous Alumina with Large-Size Pores in Phosphoric Acid Solution. *Jpn. J. Appl. Phys.* **1998**, *37*, L1340.
(47) Masuda, H.; Fukuda, K. Ordered Metal Nanohole Arrays Made by a Two-Step Replication of Honeycomb Structures of Anodic Alumina. *Science* **1995**, *268*, 1466−1468.
(48) Linpé, W.; Harlow, G. S.; Larsson, A.; Abbondanza, G.; Rämisch, L.; Pfaff, S.; Zetterberg, J.; Evertsson, J.; Lundgren, E. An electrochemical cell for 2-dimensional surface optical reflectance during anodization and cyclic voltammetry. *Rev. Sci. Instrum.* **2020**, *91*, 044101.
(49) Linpé, W.; Harlow, G. S.; Evertsson, J.; Hejral, U.; Abbondanza, G.; Lenrick, F.; Seifert, S.; Felici, R.; Vinogradov, N. A.; Lundgren, E. The State of Electrodeposited Sn Nanopillars within Porous Anodic Alumina from in Situ X-ray Observations. *ACS Appl. Nano Mater.* **2019**, *2*, 3031−3038.
(50) Vinogradov, N. A.; Harlow, G. S.; Carlà, F.; Evertsson, J.; Rullik, L.; Linpé, W.; Felici, R.; Lundgren, E. Observation of Pore Growth and Self-Organization in Anodic Alumina by Time-Resolved X-ray Scattering. *ACS Appl. Nano Mater.* **2018**, *1*, 1265−1271.
(51) Evertsson, J.; Vinogradov, N. A.; Harlow, G. S.; Carlà, F.; McKibbin, S. R.; Rullik, L.; Linpé, W.; Felici, R.; Lundgren, E. Self-organization of porous anodic alumina films studied in situ by grazing-incidence transmission small-angle X-ray scattering. *RSC Adv.* **2018**, *8*, 18980−18991.
(52) Carlà, F.; Loglio, F.; Resta, A.; Felici, R.; Lastraioli, E.; Innocenti, M.; Foresti, M. L. Electrochemical Atomic Layer Deposition of CdS on Ag Single Crystals: Effects of Substrate Orientation on Film Structure. *J. Phys. Chem. C* **2014**, *118*, 6132−6139.
(53) Sauer, G.; Brehm, G.; Schneider, S.; Nielsch, K.; Wehrspohn, R. B.; Choi, J.; Hofmeister, H.; Gösele, U. Highly ordered monocrystalline silver nanowire arrays. *J. Appl. Phys.* **2002**, *91*, 3243−3247.
(54) Durovic, M. D.; Puchta, R.; Bugarcic, Z. D.; van Eldik, R. Studies on the reactions of [AuCl4]- with different nucleophiles in aqueous solution. *Dalton Trans.* **2014**, *43*, 8620−8632.
(55) Le Penven, R.; Levason, W.; Pletcher, D. Studies of the electrodeposition of palladium from baths based on [Pd(NH3)2X2] salts. I. [Pd(NH3)2Cl2] baths. *J. Appl. Electrochem.* **1990**, *20*, 399−404.
(56) Nicklin, C.; Arnold, T.; Rawle, J.; Warne, A. Diamond beamline I07: a beamline for surface and interface diffraction. *J. Synchrotron Radiat.* **2016**, *23*, 1245−1253.
(57) Marchal, J.; Horswell, I.; Willis, B.; Plackett, R.; Gimenez, E. N.; Spiers, J.; Ballard, D.; Booker, P.; Thompson, J. A.; Gibbons, P.; Burge, S. R.; Nicholls, T.; Lipp, J.; Tartoni, N. EXCALIBUR: a small-pixel photon counting area detector for coherent X-ray diffraction - Front-end design, fabrication and characterisation. *J. Phys.: Conf. Ser.* **2013**, *425*, 062003.
(58) Kraft, P. PILATUS 2M: A detector for small angle X-ray scattering. Ph.D. Thesis, ETH Zurich, 2010.
(59) Abbondanza, G.; Larsson, A.; Carlá, F.; Lundgren, E.; Harlow, G. S. Quantitative powder diffraction using a (2 + 3) surface diffractometer and an area detector. *J. Appl. Crystallogr.* **2021**, *54*, 1140−1152.
(60) Ashiotis, G.; Deschildre, A.; Nawaz, Z.; Wright, J. P.; Karkoulis, D.; Picca, F. E.; Kieffer, J. The fast azimuthal integration Python library: *pyFAI*. *J. Appl. Crystallogr.* **2015**, *48*, 510−519.
(61) Abràmoff, M. D.; Magalhães, P. J.; Ram, S. J. Image processing with ImageJ. *Biophot. Int.* **2004**, *11*, 36−42.
(62) Carter, C. B.; Williams, D. B. *Transmission Electron Microscopy: Diffraction, Imaging, and Spectrometry*; Springer, 2016.
(63) Keller, F.; Hunter, M. S.; Robinson, D. L. Structural Features of Oxide Coatings on Aluminum. *J. Electrochem. Soc.* **1953**, *100*, 411.
(64) Li, A. P.; Müller, F.; Birner, A.; Nielsch, K.; Gösele, U. Hexagonal pore arrays with a 50−420 nm interpore distance formed by self-organization in anodic alumina. *J. Appl. Phys.* **1998**, *84*, 6023−6026.
(65) Meng, G.; Jung, Y. J.; Cao, A.; Vajtai, R.; Ajayan, P. M. Controlled fabrication of hierarchically branched nanopores, nanotubes, and nanowires. *Proc. Natl. Acad. Sci. U.S.A.* **2005**, *102*, 7074−7078.
(66) Toby, B. H.; Von Dreele, R. B. *GSAS-II*: the genesis of a modern open-source all purpose crystallography software package. *J. Appl. Crystallogr.* **2013**, *46*, 544−549.
(67) Shin, H. S.; Yu, J.; Song, J. Y.; Park, H. M.; Kim, Y.-S. Origins of size-dependent lattice dilatation in tetragonal Sn nanowires: Surface stress and growth stress. *Appl. Phys. Lett.* **2010**, *97*, 131903.


https://doi.org/10.1021/acsanm.3c05487
*ACS Appl. Nano Mater.* 2024, 7, 3861−3872

(68) Batchelder, D. N.; Simmons, R. O. X-Ray Lattice Constants of Crystals by a Rotating-Camera Method: Al, Ar, Au, CaF2, Cu, Ge, Ne, Si. *J. Appl. Phys.* **1965**, *36*, 2864−2868.
(69) Dutta, B. N.; Dayal, B. Lattice Constants and Thermal Expansion of Palladium and Tungsten up to 878 °C by X-Ray Method. *Phys. Status Solidi B* **1963**, *3*, 2253−2259.
(70) Denton, A. R.; Ashcroft, N. W. Vegard's law. *Phys. Rev. A: At., Mol., Opt. Phys.* **1991**, *43*, 3161−3164.
(71) Dunn, C.; Kogh, E. Comparison of dislocation densities of primary and secondary recrystallization grains of Si-Fe. *Acta Metall.* **1957**, *5*, 548−554.
(72) Kuk, Y.; Feldman, L.; Silverman, P. Epitaxial Growth of Au on Pd (111). Ph.D. Thesis, American Vacuum Society, 1983.
(73) Matthews, J.; Jackson, D.; Chambers, A. Effect of coherency strain and misfit dislocations on the mode of growth of thin films. *Thin Solid Films* **1975**, *26*, 129−134.
(74) Newville, M.; Stensitzki, T.; Allen, D. B.; Rawlik, M.; Ingargiola, A.; Nelson, A. *Lmfit: Non-linear Least-Square Minimization and Curve-Fitting for Python*; Astrophysics Source Code Library, record ascl:1606.014, 2016.
(75) Sun, C. Q. Size dependence of nanostructures: Impact of bond order deficiency. *Prog. Solid State Chem.* **2007**, *35*, 1−159.
(76) Leontyev, I. N.; Kuriganova, A. B.; Leontyev, N. G.; Hennet, L.; Rakhmatullin, A.; Smirnova, N. V.; Dmitriev, V. Size dependence of the lattice parameters of carbon supported platinum nanoparticles: X-ray diffraction analysis and theoretical considerations. *RSC Adv.* **2014**, *4*, 35959−35965.
(77) Osteryoung, J. G.; Schreiner, M. M. Recent Advances in Pulse Voltammetry. *CRC Crit. Rev. Anal. Chem.* **1988**, *19*, S1−S27.





https://doi.org/10.1021/acsanm.3c05487
*ACS Appl. Nano Mater.* 2024, 7, 3861−3872